

See discussions, stats, and author profiles for this publication at: <https://www.researchgate.net/publication/262728356>

# Elucidation of the $\text{Na}_{2/3}\text{FePO}_4$ and $\text{Li}_{2/3}\text{FePO}_4$ Intermediate Superstructure Revealing a Pseudouniform Ordering in 2D

ARTICLE *in* JOURNAL OF THE AMERICAN CHEMICAL SOCIETY · MAY 2014

Impact Factor: 12.11 · DOI: 10.1021/ja503622y

CITATIONS

8

READS

80

## 5 AUTHORS, INCLUDING:



**Florent Boucher**

University of Nantes, CNRS

122 PUBLICATIONS 1,439 CITATIONS

SEE PROFILE



**Joel Gaubicher**

French National Centre for Scientific Resea...

72 PUBLICATIONS 1,274 CITATIONS

SEE PROFILE



**Marine Cuisinier**

Qatar Environment and Energy Research In...

26 PUBLICATIONS 538 CITATIONS

SEE PROFILE



**Philippe Moreau**

Université de Nantes, CNRS

98 PUBLICATIONS 1,208 CITATIONS

SEE PROFILE

# Elucidation of the $\text{Na}_{2/3}\text{FePO}_4$ and $\text{Li}_{2/3}\text{FePO}_4$ intermediate superstructure revealing a pseudouniform ordering in 2D

Florent Boucher,<sup>\*,†,‡</sup> Joël Gaubicher,<sup>†,‡</sup> Marine Cuisinier,<sup>†,§</sup> Dominique Guyomard,<sup>†,‡</sup> and Philippe Moreau<sup>†,‡</sup>

<sup>†</sup>*Institut des Matériaux Jean Rouxel (IMN), Université de Nantes - CNRS, UMR 6502, 2 rue de la Houssinière, BP 32229, 44322 Nantes cedex 3, France*

<sup>‡</sup>*Réseau sur le Stockage Electrochimique de l'Energie (RS2E), FR CNRS 3459, France*

**KEYWORDS:** olivine, Na-ion battery, charge ordering, vacancy ordering, superstructure, DFT calculations.

---

**ABSTRACT:** Based on TEM, synchrotron X-ray diffraction, DFT calculations and Mössbauer spectroscopy, a unified understanding of the Na and Li intercalation process in  $\text{FePO}_4$  is proposed. The key to this lies in solving the highly sought-after intermediate  $\text{A}_{2/3}\text{FePO}_4$  ( $\text{A}=\text{Na}, \text{Li}$ ) superstructures that are characterized by alkali ions as well as  $\text{Fe}^{\text{II}}/\text{Fe}^{\text{III}}$  charge orderings in a monoclinic 3-fold supercell. Formation energies and electrochemical potential calculations confirm that  $\text{Na}_{2/3}\text{FePO}_4$  and  $\text{Li}_{2/3}\text{FePO}_4$  are stable and metastable, respectively, and that they yield insertion potentials in fair agreement with experimental values. The 2/3 Na(Li) and 1/3 vacancy sublattice of the intermediate phases forms a dense  $(10\bar{1})_{\text{Pnma}}$  plane in which the atom/vacancy ordering is very similar to that predicted for the most uniform distribution of 1/3 of vacancies in a 2D square lattice. Structural analysis strongly suggests that the key role of this dense plane is to constrain the intercalation in the diffusion channels to operate by cooperative filling of  $(\text{bc})_{\text{Pnma}}$ . From a practical point of view, this generalized mechanism highlights the fact that an interesting strategy for obtaining high rate  $\text{FePO}_4$  materials would consist in designing grains with an enhanced (101) surface area, thereby offering potential for substantial improvements with respect to the performance of rechargeable Li and Na batteries.

---

## INTRODUCTION

At a time when the first mass-produced electrical vehicles are about to be launched, the various active materials being used for positive electrodes of lithium-ion batteries are still vying for first place. The pros and cons of these materials involve performance evaluation with respect to capacity, power, cycle life, non-toxicity, safety and cost.<sup>1</sup> For more than 15 years,  $\text{LiFePO}_4$  has remained one of the most attractive candidates by virtue of its remarkably good performance in most of these areas. One of its particularly striking qualities is its high power capability,<sup>2</sup> although both end members,  $\text{LiFePO}_4$  and  $\text{FePO}_4$ , are insulators.<sup>3</sup> Even though Li ion diffusion has since been proven to be fairly high, and even if intrinsic low conductivity limitations have been overcome by the use of carbon coating<sup>4</sup> and nanostructuring,<sup>5,6</sup> there is still much debate about the actual intercalation process at work.<sup>7–14</sup> It is hoped

that a thorough understanding of this process may lead to the synthesis of optimized  $\text{LiFePO}_4$  materials and provide us with guidelines for selecting potentially significant new phases.<sup>14</sup>

One of the most astute insights into this process to date was proposed by Delmas *et al.* and is referred to as the “domino-cascade” model.<sup>13</sup> This model explains the standard observation of the coexistence of fully intercalated and fully deintercalated individual particles, and provides the driving force behind this sort of physical separation of the two end member phases: the minimization of interfacial constraints within each individual grain. During deintercalation, the lithium channels are rapidly emptied within **bc** planes of the orthorhombic structure, with the deintercalation progressing in the direction of successive **bc** planes (i. e. the **a** direction). A distorted zone, limited in time and space, is assumed between

the two phases, thus allowing the easy migration of ions and electrons.

This model was further confirmed by various local techniques (diffraction, EELS, XPS, e.g. ),<sup>15–18</sup> showing that the crystals within powders of intermediate  $\text{Li}_x\text{FePO}_4$  ( $0 < x < 1$ ) compositions are usually found to be either fully intercalated or not yet intercalated. All these studies are however referring to final *ex situ* analyses, and do not rule out transition states far from the end result. The swiftness of the intercalation process hampers the observation of potentially more complex intercalation paths, as suggested recently by Malik et al.<sup>17</sup> By combining Monte Carlo simulations with *ab initio* density functional theory calculations, they came to the conclusion that the remarkable rate capability of  $\text{LiFePO}_4$  can be explained by the existence of an alternative single-phase transformation path, accessible at low overpotential. This alternative path precludes the need to go through the slow nucleation and growth mechanism suggested by the *ex situ* experiments.

We recently established that  $\text{NaFePO}_4$  can be obtained in a sodium battery, although with much slower kinetics, and that  $\text{NaFePO}_4$  exhibits the same olivine structure type as  $\text{LiFePO}_4$ .<sup>16</sup> Despite the fact that during the first discharge (intercalation of sodium ions) of a  $\text{FePO}_4/\text{Na}$  battery a seemingly single plateau was observed, during the subsequent charge (deintercalation), two electrochemical processes were clearly evidenced. The existence of an intermediate composition close to  $\text{Na}_{0.7}\text{FePO}_4$  was proven, and this intermediate phase was recently identified as an ordered  $\text{Na}_{2/3}\text{FePO}_4$  composition.<sup>19,20</sup> The link to the double electrochemical process, consisting in a two-phase process between  $0 < x < 2/3$  and a single-phase process between  $2/3 < x < 1$ , was established. However, unlike the  $\text{Li}_x\text{FePO}_4$  system, thorough reassessment of the phase diagram of  $\text{Na}_x\text{FePO}_4$  should be considered under dynamic conditions within an operating Na battery. Vastly extended limits of solubility were indeed observed from *operando* XRD.<sup>21</sup> These correspond to variations in the lattice volumes during the phase transformation, which account for the entering of Na occupancies ( $\tau(\text{Na})$ ) into the thermodynamically forbidden composition  $\text{Na}_{0.05}\text{FePO}_4$  -  $\text{Na}_{2/3}\text{FePO}_4$ . The direct consequence of this dynamically smoothed phase trans-

formation is a reduced volume mismatch that should allow for the accommodation of the larger size of  $\text{Na}^+$ . The strong similarities, yet clear differences, between the Li and Na batteries motivated further comparative studies of both systems. Many questions arose, such as: Aside from the characteristic merit of the sodium iron phosphate system itself,<sup>16,20,22–28</sup> could this comparison assist in further improving our knowledge of the chemical insertion process of  $\text{LiFePO}_4$ ? In particular, why are certain compositions in  $\text{Li}_x\text{FePO}_4$  stabilized from high to low temperature?<sup>15</sup> Could knowledge of the  $\text{Na}_{2/3}\text{FePO}_4$  superstructure be useful for interpreting the recent observation of a metastable  $\text{Li}_x\text{FePO}_4$  phase?<sup>29</sup> Do we slow down the fast lithium insertion process in case of sodium ions and in doing so find out how it really proceeds? Lastly, could our experience with Li compounds help us to improve Na ion technology?

In order to reach a precise understanding of the Li/Na intercalation process, the elucidation of the intermediate phase of the  $\text{Na}_{2/3}\text{FePO}_4$  composition is essential. The mean atomic structure of this phase has already been presented,<sup>16</sup> but small extra peaks remained unexplained while using the mean Pnma structure.<sup>20,25,30</sup> To date, two groups have tried to elucidate the superstructure of the  $\text{Na}_{2/3}\text{FePO}_4$  phase but neither of them were able to propose any realistic model for the Na/vacancy ordering. By combining electron diffraction and X-Ray diffraction, Casas-Cabanas *et al.*<sup>25</sup> revealed various kinds of superstructures that were justified as being the direct consequence of a slight difference in Na content. Very recently, by using a combination of X-Ray diffraction, Mössbauer spectroscopy, and density functional theory (DFT) calculations, Lu *et al.*<sup>20</sup> have shown the existence of three kinds of iron sites for this  $\text{Na}_{2/3}\text{FePO}_4$  composition, with one  $\text{Fe}^{\text{III}}$  site and two  $\text{Fe}^{\text{II}}$  sites. They concluded, however, that one of the  $\text{Fe}^{\text{II}}$  sites corresponds to a highly distorted site. The objective of the present study is thus to fully characterize, for the first time, the superstructure found in  $\text{Na}_{2/3}\text{FePO}_4$ , by using a combination of electron diffraction, X-Ray synchrotron diffraction, Mössbauer spectroscopy, and DFT calculations. The structural model that we put forward, including consistent Na/vacancy and  $\text{Fe}^{\text{II}}/\text{Fe}^{\text{III}}$  orderings, allows for the proposal of a cationic insertion/deinsertion mechanism in the  $\text{A}_x\text{FePO}_4$  system.

## EXPERIMENTAL METHOD

**Electrochemical synthesis.** The  $\text{Na}_{2/3}\text{FePO}_4$  intermediate composition was electrochemically synthesized, as previously described,<sup>16</sup> by using a positive electrode made with a mixture of 70%  $\text{FePO}_4$  (olivine) and 30% carbon black (Ketjen).  $\text{FePO}_4$  was obtained from  $\text{LiFePO}_4$  by chemical oxidation in acetonitrile, using  $\text{NO}_2\text{BF}_4$  (Aldrich). The mixture was then ball-milled (30 min, 500 rpm, silicon nitride ceramic balls) and pasted onto an Al current collector. Electrodes and powders were kept in a dry argon glove box to avoid any side reactions of the  $\text{FePO}_4$  with air. Swagelok<sup>TM</sup>-type batteries were mounted with sodium as the negative and reference electrode, and 1M  $\text{NaClO}_4$  in propylene carbonate as the electrolyte. Batteries were cycled in potentiodynamic mode (PITT, VMP-Biologic SA, Claix, France), with step duration being restricted by a current limit. The latter was set to be equivalent to nominal 1 Na/200 h. The  $\text{Na}_{2/3}\text{FePO}_4$  phase was obtained with high precision ( $x=0.66$ ) during the charge of the battery by equilibrating the sample at 2.95V versus Na/Na<sup>+</sup>. The  $\text{Na}_{2/3}\text{FePO}_4$  sample not being sensitive to air, no specific apparatus was used for the various transfers.

**TEM and electron diffraction.** Operated at 100 kV in order to limit beam damage, a Hitachi HF2000 transmission electron microscope was used to obtain images and diffraction patterns in micro-diffraction mode. Powders obtained from the electrochemical cells were deposited onto a holey carbon grid, which was then placed onto a double tilt cold sample holder. Experiments were carried out at liquid nitrogen temperature. Diffraction pattern indexations and simulations were performed using the JEMS program.<sup>31</sup>

**Synchrotron X-ray diffraction.** Experiments were performed at SOLEIL, the French third-generation synchrotron radiation source on the CRISTAL beamline. A monochromatic beam with  $\lambda = 0.725633 \text{ \AA}$  was used and shone onto a sealed capillary ( $\varnothing 0.5 \text{ mm}$ ), inside which the powder was placed. The diffracted intensities were measured in transmission geometry ( $4.7 \leq 2\theta \leq 33.7$ ) using a Mar image plate detector, allowing an optimal signal to noise ratio. A  $\text{LaB}_6$  powder sample was used for calibrating the Mar detector and determining the peak shape resolution of the apparatus. For temper-

ature-dependent experiments, the capillary was heated in steps of 25°C using a calibrated high-temperature gas flow. Rietveld analyses were achieved by using the FullProf Suite software. Since the superstructure corresponding to the Na/vacancy ordering only generates a few additional diffraction peaks, a few constraints had to be applied to the structural refinement in order to avoid divergences and inconsistencies. Similarity was imposed with respect to isotropic displacement parameters for a given atomic species, and they were furthermore fixed in the case of oxygen atoms ( $B_{\text{iso}}=0.25 \text{ \AA}^2$ ). Additionally, soft constraints were used on the P-O bond lengths (1.53(1)  $\text{\AA}$ ). In this manner, correlation coefficients were maintained below 87 % and all of the atomic coordinates were able to be refined. Angular-dependent shapes of the diffracted intensities were fitted using a Thompson-Cox-Hastings pseudo-Voigt function. Selective size-broadening parameters were used for the supercell reflections ( $h = 3n \pm 1$  &  $h = 3n \pm 2$ ) in order to accommodate the smaller coherence length associated with the Na/vacancy ordering.

**Mössbauer spectroscopy.** The  $^{57}\text{Fe}$  Mössbauer spectra were collected in transmission geometry with a constant acceleration spectrometer using a  $^{57}\text{Co}$   $\gamma$ -ray source in a Rh matrix equipped with a cryostat. Velocity and isomer shift (IS) calibrations were performed using  $\alpha\text{-Fe}$  as a standard at room temperature. Quadrupole splitting (QS) data on each type of Fe ion were analyzed as discrete distributions of 0.1  $\text{mm.s}^{-1}$  steps in the range 0 to 6  $\text{mm.s}^{-1}$ , and then fitted with Gaussians.

**Electronic structure calculations.** Ground-state electronic structures of  $\text{Li}_{2/3}\text{FePO}_4$  and  $\text{Na}_{2/3}\text{FePO}_4$  were obtained within the DFT formalism by using the Perdew-Burke-Ernzerhof parameterization of the generalized gradient approximation (PBE-GGA).<sup>32</sup> A GGA+U with  $U_{\text{eff}}=4.3\text{eV}$  was used to better describe the correlation on the Fe 3d orbitals.<sup>3</sup> Cell parameters were taken from experimental values, while the atomic positions were optimized by minimizing atomic forces. The structural relaxation was carried out with the *ab initio* total energy and molecular dynamics program, VASP (Vienna *ab initio* simulation package).<sup>33</sup> Projector augmented-wave (PAW) pseudopotentials<sup>34,35</sup> were used: standard PAW were chosen for O (PAW\_PBE O:  $2s^22p^4$ ) and P (PAW\_PBE P:  $3s^23p^3$ ) but

semicore states were included for Li (PAW\_PBE Li\_sv:  $1s^2 2s^1$ ), Na (PAW\_PBE Na\_pv:  $2p^6 3s^1$ ), and Fe (PAW\_PBE Fe\_pv:  $3p^6 3d^7 4s^1$ ). A cut-off of 600 eV for the plane wave expansion and a  $(2 \times 8 \times 4)$  Monkhorst-Pack  $k$ -points mesh (16  $k$ -points in the irreducible part of the Brillouin zone) were necessary in order to reach the convergence of the Hellmann-Feynman forces. Atomic positions were relaxed so as to minimize those forces down to  $0.02 \text{ eV/\AA}$ . In a second step, using the resulting optimized  $\text{Na}_{2/3}\text{FePO}_4$  structure,  $^{57}\text{Fe}$  Mössbauer parameters (QS and IS) were deduced from the calculation of the electric field gradient tensors around the Fe sites and from the contact charge densities at the Fe nuclei. To improve accuracy, those quantities were obtained from the full potential linearized augmented plane wave (FLAPW) method, as embodied in the WIEN2k package.<sup>36</sup>

The size of the basis set was defined by  $\text{RMT} \times K_{\text{MAX}} = 7.5$  using the following muffin tin radii ( $\text{\AA}$ ): 1.14, 1.06, 0.77 and 0.74 for Na, Fe, P and O, respectively. The same  $(2 \times 8 \times 4)$   $k$ -points mesh was used for the electronic self-consistency. The QS, expressed as a Doppler velocity (mm/s), was calculated from  $V_{zz}$  (the largest component of the electric field gradient (EFG) tensor) using the expression:<sup>37</sup>

$$QS[\text{mm/s}] = 10^{-4} \frac{c[m/s]Q[b]}{2E_\gamma[\text{eV}]} V_{zz}[10^{21} \text{V/m}^2]$$

where  $c$  is the speed of light,  $E_\gamma$  is the energy of the emitted  $\gamma$  radiation of the  $^{57}\text{Fe}$  nucleus, and  $Q$  is the quadrupole moment of the Fe nucleus. Considering  $Q_{Fe} = 0.16b$ ,<sup>38</sup> this leads to:<sup>37</sup>

$$QS[\text{mm/s}] = 0.1617 \times V_{zz}[10^{21} \text{V/m}^2]$$

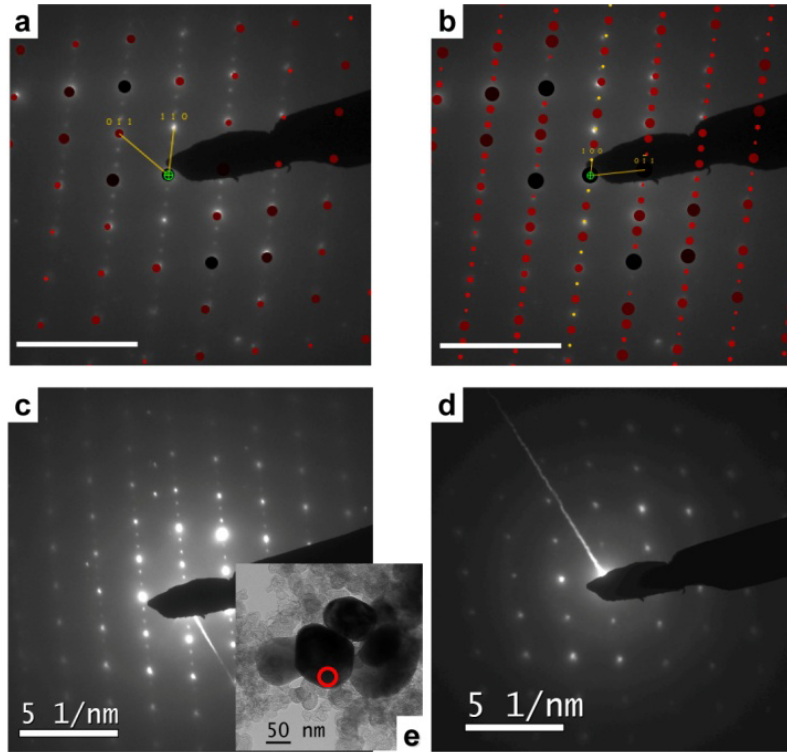


**Figure 1.** TEM diffraction patterns of  $\text{Na}_{2/3}\text{FePO}_4$  at liquid nitrogen temperature. (a) Pattern obtained along the  $[\bar{1}\bar{1}\bar{1}]_{\text{Pnma}}$  zone axis. The same pattern is indexed in (b) considering the  $\text{P2}_1/\text{n}$  monoclinic cell ( $[011]_{\text{P2}_1/\text{n}}$  zone axis). Simulated patterns using the JEMS program are superimposed. Scale markers represent  $5 \text{ nm}^{-1}$ . (c) Pattern obtained along the  $[\bar{1}\bar{1}\bar{1}]_{\text{Pnma}}$  zone axis before irradiation. (d) Same position as (c) but after a two minute irradiation. (e) TEM image of the powder where the red circle indicates the area chosen for diffraction patterns (c) and (d). Neither beam damages nor changes in the cell parameters can be visualized on the crystal.

The IS of the emitted  $\gamma$  radiation for the  $^{57}\text{Fe}$  nucleus was determined from the calculation of electron contact densities and comparison with respect to a reference compound. The

calibration procedure presented by Wdowik *et al.*<sup>39</sup> was used. Thus, for an  $^{57}\text{Fe}$  nucleus in a given  $A$  compound, the IS with respect to the standard  $\alpha\text{-Fe}$  is given by:

$$IS_A - IS_{Fe}[mm/s] = -0.291 (\rho_A - \rho_{Fe})[a.u.^{-3}]$$

where  $\rho_A$  and  $\rho_{Fe}$  are the electron contact densities on the  $^{57}\text{Fe}$  nucleus for the given A compound and the  $\alpha\text{-Fe}$  reference, respectively. These contact densities are calculated by averaging the electron density inside the region near the nucleus where the radius is  $R_0=4.987$  fm.<sup>39</sup>

## RESULTS AND DISCUSSION

**Electron diffraction experiments.** In order to identify the possible superstructure responsible for the extra diffraction peaks, electron diffraction patterns in a transmission electron microscope (TEM) were obtained on various  $\text{Na}_{2/3}\text{FePO}_4$  crystals in different orientations. Room temperature TEM experiments confirmed that extra spots were indeed present, although they appeared to be quite unstable under the electron beam. Only at liquid nitrogen temperature, were the extra spots preserved long enough to allow zone axis alignment. Diffraction patterns revealed a 3-fold superstructure in the  $[110]$  direction of the pristine Pnma lattice (Figure 1a), which lead us to consider a monoclinic cell (Figure 2) such that:

$$\begin{pmatrix} a \\ b \\ c \end{pmatrix}_{\text{mono}} = \begin{pmatrix} 0 & 3 & 0 \\ 0 & 0 & 1 \\ 1 & -1 & 0 \end{pmatrix} \begin{pmatrix} a \\ b \\ c \end{pmatrix}_{\text{Pnma}}$$

Allowing for minor adjustments of the cell parameters values, all spots of the electron diffraction patterns could then be indexed using this new set of parameters (Figure 1b). In their experiments, Casas-Cabanas *et al.*,<sup>25</sup> also found the existence of additional spots, but were not able to index all of them using a unique supercell. Their experiments were, however, realized at room temperature using an acceleration voltage of 300 kV, which may have been unfavorable with respect to avoiding knock-on damage or Na/vacancy reorganization. Indeed, their conclusion showed a range of stable compositions with different Na/vacancy arrangements.

**X-Ray synchrotron diffraction.** Intensity being unreliable in these electron diffraction experiments, a full atomic description of the structure was obtained after acquisition of X-Ray diffraction (XRD) patterns on the SOLEIL synchrotron. Firstly, making use of a whole-powder-pattern fitting procedure, these XRD measurements were qualitatively fitted by using the approximate supercell parameters as an initial estimation.

Then different structural models were evaluated by considering the group to subgroup relations of the Pnma space group that are compatible with the matrix transformation given above. Atomic parameters for the superstructure were deduced from the average unit cell analysis of the  $\text{Na}_{0.7}\text{FePO}_4$  structure.<sup>16</sup> A very satisfactory Rietveld refinement was obtained (Figure 3) considering the monoclinic  $\text{P2}_1/\text{n}$  space group. This lead to the structure presented in Figure 2, with the following cell parameters:  $a = 18.2374(3)$  Å,  $b = 4.9369(1)$  Å,  $c = 11.9609(3)$  Å,  $\beta = 120.722(2)^\circ$ . All structural data are given in Table 1 and in the Supporting Information.

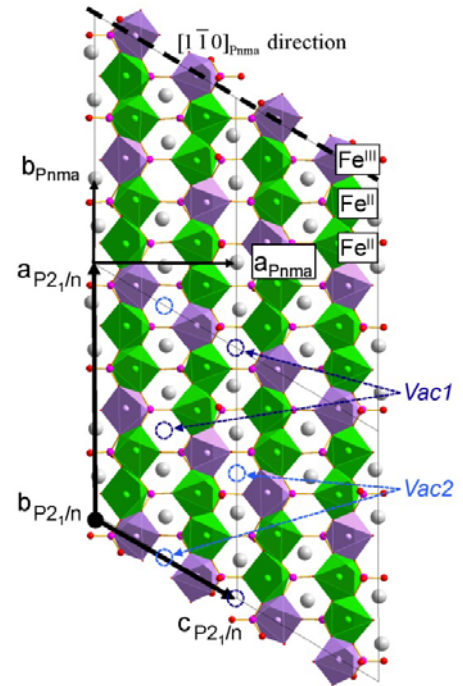


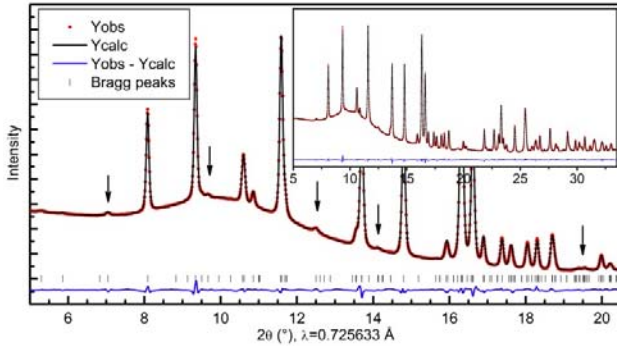
**Figure 2.** Structure of  $\text{Na}_{2/3}\text{FePO}_4$  phase viewed along the  $b_{\text{P21/n}}$  direction, which is equivalent to the  $c_{\text{Pnma}}$  one (not shown). P-O bonds of  $\text{PO}_4$  tetrahedra are shown, with oxygen atoms in red and phosphorus atoms in pink.  $\text{FeO}_6$  octahedra are represented in light green ( $\text{Fe}^{\text{II}}$ ), and purple ( $\text{Fe}^{\text{III}}$ ). Sodium atoms (in light grey) are situated in the channels along the  $a_{\text{P21/n}}$  direction. The superstructure appears in this direction with two filled sodium sites for one empty site. This ordering can also be evidenced in the  $[1\bar{1}0]_{\text{Pnma}}$  direction as illustrated. Charge ordering defines alternating  $(bc)_{\text{P21/n}}$   $\text{Fe}^{\text{II}}$  planes, and  $\text{Fe}^{\text{III}}$  planes.

In the channel direction ( $b_{\text{Pnma}}$ ), this being the preferred diffusion path for sodium atoms by analogy with the lithium equivalent,<sup>15,40</sup> two sodium atoms are separated by one empty site. This leads to the  $\text{Na}_{2/3}\text{FePO}_4$  composition. The ordering in the neighboring channels is found to be shifted in the  $c$  direction ( $[1\bar{1}0]$  Pnma direction, Figure 2).

**Table 1.** Experimentally refined (left part) and DFT optimized (right part) atomic parameters for  $\text{Na}_{2/3}\text{FePO}_4$ .

Experimentally refined structure <sup>a</sup>						DFT optimized structure <sup>a</sup>				
Atom	x	y	z	Uiso(Å <sup>2</sup> )	BVS <sup>b</sup>	x	y	z	shifts(Å) <sup>c</sup>	BVS <sup>b</sup>
Fe1	0.1503(4)	0.9687(16)	0.2151(6)	0.0056(5)	2.01	0.1562	0.9893	0.2178	0.14	2.01
Fe2	0.5077(4)	0.013(2)	0.7864(7)	0.0056	2.91	0.5099	0.0064	0.7837	0.07	3.01
Fe3	0.8247(5)	0.0014(12)	0.2186(7)	0.0056	2.04	0.8240	0.9771	0.2203	0.12	2.01
Na1	0.6598(7)	0.974(3)	0.5219(10)	0.012(2)	1.01	0.6579	0.9840	0.5132	0.10	0.99
Na2	0.8427(10)	0.012(4)	0.5032(16)	0.012	1.00	0.8402	0.9879	0.5024	0.13	0.99
P1	0.2146(6)	0.4518(16)	0.3945(8)	0.0046(7)	5.07	0.2157	0.4513	0.3987	0.04	4.97
P2	0.4523(5)	0.5683(16)	0.6113(7)	0.0046	5.01	0.4572	0.5699	0.6107	0.09	5.00
P3	0.8829(5)	0.4377(17)	0.3968(8)	0.0046	4.94	0.8861	0.4297	0.3966	0.07	5.01
O1	0.2185(14)	0.751(2)	0.372(3)	0.0032	-2.21	0.2166	0.7608	0.3956	0.31	-2.06
O2	0.462(2)	0.260(2)	0.624(3)	0.0032	-2.02	0.4603	0.2621	0.6301	0.09	-2.07
O3	0.8755(18)	0.747(2)	0.393(2)	0.0032	-1.91	0.8786	0.7369	0.3832	0.16	-2.04
O4	0.0962(17)	0.131(4)	0.0360(11)	0.0032	-1.87	0.0886	0.1468	0.0328	0.14	-2.02
O5	0.5715(16)	0.829(4)	0.9611(13)	0.0032	-2.18	0.5665	0.8423	0.9580	0.10	-2.03
O6	0.7664(16)	0.144(6)	0.0377(13)	0.0032	-1.95	0.7666	0.1578	0.0396	0.07	-2.01
O7	0.1249(10)	0.311(5)	0.327(3)	0.0032	-1.86	0.1240	0.3226	0.3316	0.09	-1.98
O8	0.7537(16)	0.698(4)	0.687(2)	0.0032	-1.86	0.7469	0.6817	0.6809	0.13	-1.99
O9	0.7883(8)	0.334(4)	0.328(2)	0.0032	-1.87	0.7974	0.2840	0.3293	0.29	-1.96
O10	0.4083(19)	0.702(5)	0.678(3)	0.0032	-2.05	0.4123	0.7258	0.6755	0.15	-1.98
O11	0.4617(9)	0.287(4)	0.322(3)	0.0032	-2.05	0.4525	0.2962	0.3101	0.16	-1.93
O12	0.0710(17)	0.695(5)	0.667(3)	0.0032	-2.18	0.0688	0.6983	0.6727	0.10	-1.94

<sup>a</sup>P2<sub>1</sub>/n space group, experimental cell parameters:  $a = 18.2374(3)$  Å,  $b = 4.9369(1)$  Å,  $c = 11.9609(3)$  Å,  $\beta = 120.722(2)$ . See computational part for details about the DFT optimization. <sup>b</sup>Bond valence sums (BVS) calculated according to Brown and Altermatt<sup>41</sup>, and Brese and O'keeffe.<sup>42</sup> <sup>c</sup>Shifts(Å) give distances between the experimentally refined atomic positions and the DFT optimized ones.

**Figure 3.** Rietveld refinement pattern of the synchrotron X-Ray diffraction data measured for  $\text{Na}_{2/3}\text{FePO}_4$  at room temperature. Superstructure peaks are indicated by arrows.

The way in which the sodium atoms are ordered within the unit cell can be interpreted in terms of uniformity of the sodium/vacancy ordering in a 2D lattice.<sup>43</sup> We first consider the average Pnma unit cell<sup>16</sup> and the host  $\text{FePO}_4$  framework projected along the **b** axis in Figure 4a. In this average cell description, all insertion sites are partially occupied by sodium atoms. A possible ordering of sodium ions and vacancies is

related to the strengths of interactions between the Na sites. Since the strongest interactions are found in the densest atomic planes, *i.e.* the planes with the shortest Na-Na distances, we then focus on the densest atomic planes in order to better describe the ordering. Excluding the **bc** plane, which is the densest plane in the olivine phases and is implied in the domino-cascade model ( $d_{\text{Na-Na}} = 3.04$  Å along **b** and  $d_{\text{Na-Na}} = 4.94$  Å along **c**), the next densest atomic plane is  $(10\bar{1})_{\text{Pnma}}$ . The  $(10\bar{1})_{\text{Pnma}}$  plane, shown in Figure 4a, defines a regular lattice with  $d_{\text{Na-Na}} = 3.04$  Å along **b**, and  $d_{\text{Na-Na}} = 5.70$  Å along the  $[101]_{\text{Pnma}}$  direction. The ordering of the vacancies observed for the monoclinic P2<sub>1</sub>/n supercell (Figure 4c) can be described within the same plane, *i.e.* the  $(0\bar{1}1)_{\text{P2}_1/\text{n}}$  (Figure 4d), where vacancies are represented as blue spheres. The distribution between sodium atoms and vacancies in  $(0\bar{1}1)_{\text{P2}_1/\text{n}}$  is very similar to the 2D distribution predicted by Gonzalez *et al.*<sup>44</sup> for the most uniform distribution of 1/3 of vacancies in a 2D



square lattice. The pseudouniform ordering they propose in 2D is a way to distribute, in the most uniform manner, the minority specie B for the system  $A_{1-x}B_x$  in a 2D square lattice, where A and B can be any kind of species.

The A and B species correspond in our case to sodium sites and vacancies, respectively, with  $x=1/3$ . As discussed at the end of the paper, the dense  $(0\bar{1}1)_{P2_1/n}$  (or  $(10\bar{1})_{Pnma}$ ) planes provide a key contribution toward understanding the ordering mechanism observed in  $\text{Na}_{2/3}\text{FePO}_4$ .

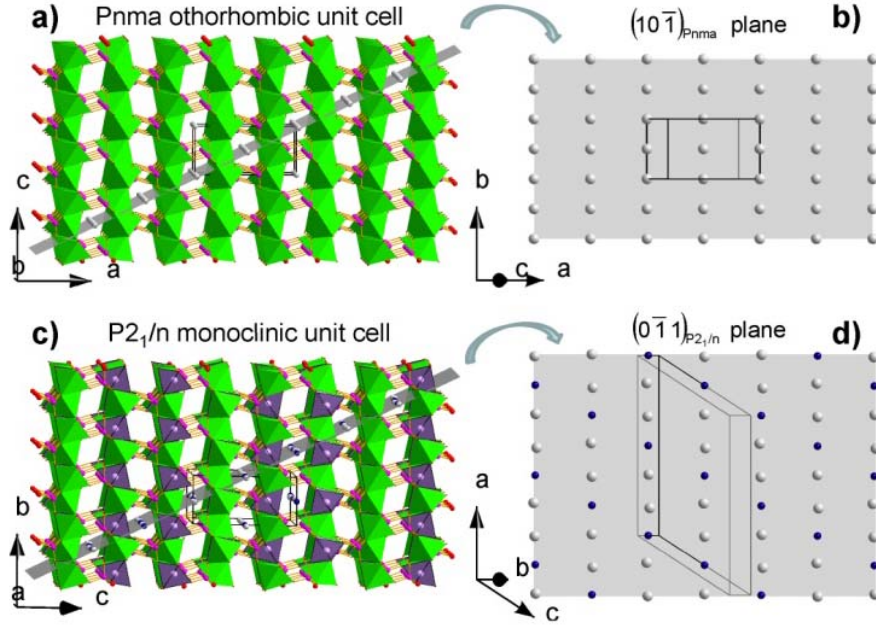


**Figure 4.** Schematic view of the host  $\text{FePO}_4$  framework revealing dense insertion planes. P-O bonds of  $\text{PO}_4$  tetrahedra are shown, with oxygen atoms in red and phosphorus atoms in pink.  $\text{FeO}_6$  octahedra are represented in light green ( $\text{Fe}^{\text{II}}$ ) and purple ( $\text{Fe}^{\text{III}}$ ). Sodium atoms and vacancies are represented in light grey and blue, respectively. (a) Projection along  $\mathbf{b}_{Pnma}$  axis showing the sodium positions in the dense intercalation plane given in (b). (c) Projection along the  $\mathbf{a}_{P2_1/n}$  axis showing the sodium and vacancy positions in the dense intercalation plane given in (d).

Calculated bond valence sums<sup>41,42</sup> (Table 1) indicate the existence of two  $\text{Fe}^{\text{II}}$  sites for one  $\text{Fe}^{\text{III}}$  site. This  $\text{Fe}^{\text{III}}$  is surrounded by less sodium atoms (or more vacancies) than the two inequivalent  $\text{Fe}^{\text{II}}$  (Figure 2). This charge ordering, which occurs along the chains of octahedra in the  $\mathbf{a}_{P2_1/n}$  (or  $\mathbf{b}_{Pnma}$ ) direction, defines two alternating ribbons of, firstly, edge-sharing  $\text{Fe}^{\text{II}}$  octahedra and, secondly,  $\text{Fe}^{\text{III}}$  octahedra in parallel  $(\mathbf{bc})_{P2_1/n}$  or  $(\mathbf{c}, \mathbf{a}-\mathbf{b})_{Pnma}$  planes (Figure 2). Two non-symmetry related vacancy sites are observed along the channels. One site (Vac1), with the shortest distance with respect to  $\text{Fe}^{\text{III}}$  sites (3.30 Å), is situated in between two  $\text{Fe}^{\text{III}}$  sites aligned along the  $[001]_{P2_1/n}$  direction. The other site (Vac2) is surrounded by four  $\text{Fe}^{\text{III}}$  sites at a distance of 3.67 Å in the  $[021]_{P2_1/n}$  and symmetry related directions. An alternation of these two types of vacancies is observed along the channels.

In the optimized structure obtained by DFT calculations, while significant adjustments of the atomic positions are observed (up to 0.3 Å for some oxygen positions, Table 1), the  $\text{Fe}^{\text{II}}/\text{Fe}^{\text{III}}$  charge ordering is confirmed. In fact, the DFT optimization allows for improvement of the quality of the atomic structure, as shown by the evolution of the BVS values for the anions. The deviation of the BVS with respect to the expected oxidation number is, at this point, below 3.5% for the oxygen atoms (and below 1% for the cations) and is more precise than the maximum deviation of 10.5% previously observed from the experimentally determined structure. The modification of the cationic environment generated by the DFT optimization is shown in Table 2, where the  $\text{FeO}_6$  and  $\text{PO}_4$  polyhedral deformations have been quantified: Baur's distortion indices,<sup>45</sup> quadratic elongations, bond angle variances, and effective coordination number.<sup>46</sup>



**Table 2.** Local environment analysis of the iron and phosphorus sites in  $\text{Na}_{2/3}\text{FePO}_4$ .

	Experiments					DFT calculations				
	<M-O> <sup>a</sup>	DIndex <sup>b</sup>	QElong <sup>c</sup>	BAngleVar <sup>c</sup>	ECoN <sup>d</sup>	<M-O> <sup>a</sup>	DIndex <sup>b</sup>	QElong <sup>c</sup>	BAngleVar <sup>c</sup>	ECoN <sup>d</sup>
Fe1	2.14	0.062	1.083	256.5	4.81	2.17	0.046	1.063	206.2	5.37
Fe2	2.11	0.037	1.054	179.0	5.55	2.05	0.029	1.046	155.0	5.73
Fe3	2.15	0.058	1.054	174.8	4.94	2.17	0.036	1.049	157.2	5.49
P1	1.54	0.011	1.0176	66.3	3.97	1.55	0.011	1.005	21.7	3.98
P2	1.54	0.005	1.007	25.7	4.00	1.55	0.015	1.008	32.5	3.96
P3	1.55	0.009	1.006	24.4	3.99	1.55	0.010	1.004	15.2	3.98

<sup>a</sup> $\langle M - O \rangle$  (in Å) is the average of the M-O bond lengths:  $\langle M - O \rangle = \frac{1}{n} \sum_{i=1}^n (M - O)_i$ . <sup>b</sup>Baur's distortion index (DIndex).<sup>45</sup> defined as  $\Delta = 1/n \sum_{i=1}^n |(M - O)_i - \langle M - O \rangle| / \langle M - O \rangle$ . <sup>c</sup>Quadratic elongations (QElong)  $\lambda = 1/n \sum_{i=1}^n ((M - O)_i / \langle M - O \rangle_0)^2$  and bond angle variances (BAngleVar, in deg<sup>2</sup>)  $\sigma^2 = 1/(m - 1) \sum_{i=1}^m (\Phi_i - \Phi_0)^2$  are given for a quantitative measure of the polyhedral deformation.<sup>46</sup> <sup>d</sup>Effective coordination number ECoN =  $\sum_{i=1}^n [1 - ((M - O)_i / l_{av})^6]$  where  $l_{av}$  is a weighted average bond length<sup>46</sup>

Concerning the  $\text{PO}_4$  tetrahedra, the  $\text{P}(1)\text{O}_4$  unit obtained by DFT optimization is presently much more regular, with distortion parameters and effective coordination number that are very similar to the two others:  $\text{P}(2)\text{O}_4$  and  $\text{P}(3)\text{O}_4$ . The distortion of the  $\text{FeO}_6$  octahedra is also very much reduced by the DFT optimization procedure with the strongest evolution being observed for the  $\text{Fe}(1)\text{O}_6$  polyhedron. The resulting effective coordination numbers are now much more realistic. This significant improvement, obtained by DFT optimization with respect to the XRD Rietveld refinement, is not surprising considering the fact that the sodium/vacancy ordering generates only very few supercell reflections which can be used in the refinement (see Figure 3). As mentioned in the experimental part, the structural refinement in the monoclinic  $\text{P}2_1/n$  space group is rather unstable, and specific adjustments were thus needed: soft constraints on the P-O bond lengths and constraints on the atomic displacement parameters. Furthermore, the modeling of those superstructure peaks necessitated the use of specific size-broadening parameters (see experimental part) leading to full width at half maximum values 6 times those of the average cell reflections. This is indicative of the problematic ordering of those sodium ions possessing a fairly small coherence length.

**Temperature dependence and thermal stability of the superstructure:** This difficulty in obtaining long-range ordering is also well-illustrated by temperature-dependent synchrotron XRD experiments. Above 100°C, an initial narrowing of the superstructure peaks (see the Supporting Information) is detected, demonstrating that constraints are too high at room

temperature (RT) to allow a perfect reorganization of the sodium ions in the channels. Up to 250°C, a gradual evolution of the cell parameters is observed (see the Supporting Information), and above this temperature superstructure peaks disappear. These results indicate a complete mobility of Na ions above that temperature. The superstructure peaks can be recovered by lowering the temperature, thereby demonstrating the stability of the  $\text{Na}_{2/3}\text{FePO}_4$  composition. This kind of phenomenon was also observed during electron diffraction experiments. Even at liquid nitrogen temperature, the superstructure was only retained for a couple of minutes under the electron beam (Figure 1 c,d). A local increase in the mobility of sodium ions is created under the electron beam, essentially due to knock-on damage.<sup>47</sup>

Electron diffraction simulations indicate that superstructure peak intensities are only partially due to the scattering factor of sodium ions in the channels, and that the octahedron distortions induced by the charge ordering contributed significantly to this intensity. The search for such superstructure peaks in the lithium equivalent,  $\text{Li}_{2/3}\text{FePO}_4$ , was thus engaged.

A  $\text{Li}_{2/3}\text{FePO}_4$  powder was obtained by the chemical delithiation of  $\text{LiFePO}_4$ . The solid solution was obtained, in the same manner as Delacourt *et al.*<sup>15</sup>, by heating the sample at 350°C. The temperature was then slowly decreased from 350°C to 210°C, followed by a rapid quenching down to room temperature. The XRD pattern on the obtained preparation revealed a non-uniform composition. However, some of the diffracted lines could be indexed, by using the cell parameters attributed by Delacourt *et al.*, to a phase named  $\text{Li}_{x1}\text{FePO}_4$

with a composition close to  $\text{Li}_{0.75}\text{FePO}_4$ . It should be mentioned that the latter composition was referring to Végard's law, which is most probably inappropriate in the case of the existence of a superstructure. Electron diffraction experiments at liquid nitrogen temperature were unsatisfactory at first due to the high sensitivity of the crystal to the electron beam.

It was thus decided to forego the alignment of crystals along a simple zone axis, a very lengthy process, and instead to search for already aligned crystals. A weak yet similar superstructure to the sodium one was finally found and, as expected, disappeared very rapidly (Figure 5).

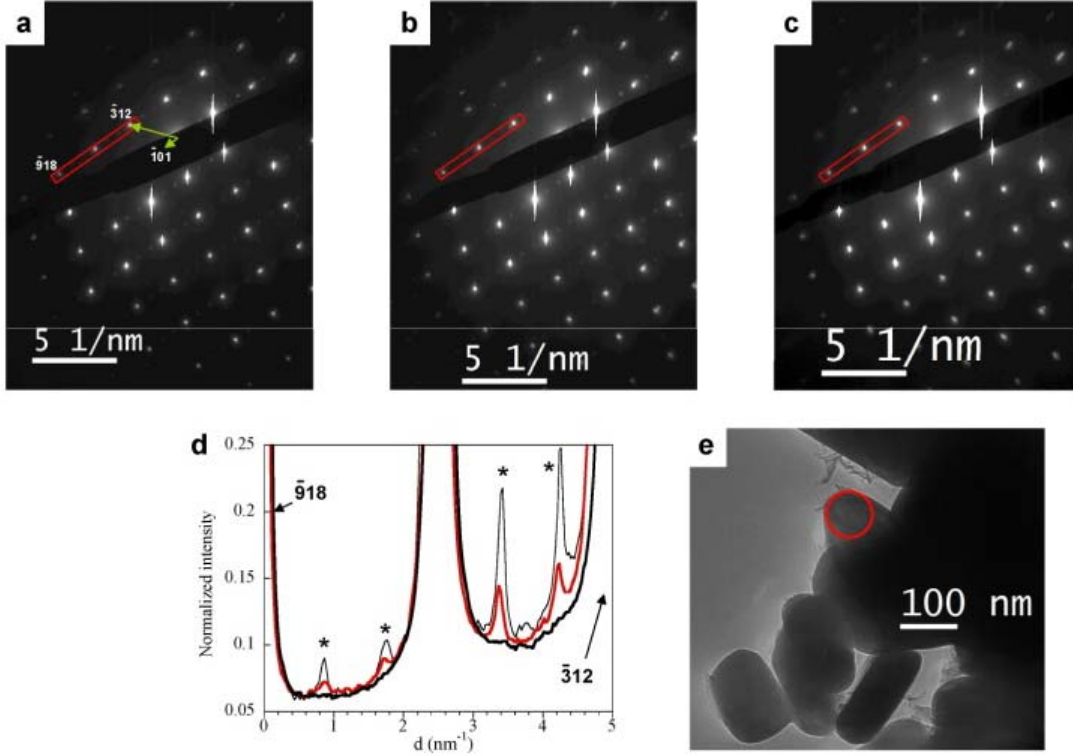


**Figure 5.** Time-dependent diffraction patterns and image of a  $\text{Li}_{2/3}\text{FePO}_4$  crystal. (a-c) Diffraction patterns along the [111] zone axis (monoclinic cell) obtained at liquid nitrogen temperature at  $t = 0\text{s}$  in (a),  $t = 45\text{s}$  in (b) and  $t = 90\text{s}$  in (c). Indexation is given in (a). (d) Intensity variation of the superstructure spots (marked with an asterisk) as a function of beam exposure time. The profiles were obtained from the same red rectangles drawn in (a-c) and the intensity normalized to the unsaturated  $(8\bar{1}1)$  peak. Thin line ( $t=0$ ), red line ( $t = 45\text{s}$ ), thick line ( $t = 90\text{s}$ ). (e) TEM image of the crystal from which the diffraction patterns were obtained. The red circle indicates the area selected for the micro-diffraction measurement.

$\text{Li}_{2/3}\text{FePO}_4$ , similarly to  $\text{Na}_{2/3}\text{FePO}_4$ , therefore presents a charge ordering of cations in the channel diffusion path. Although previously pursued,<sup>48</sup> such a superstructure was not evidenced, which was most probably due to the poor sensitivity of X-ray diffractometry to the weak intensity peaks. It should also be mentioned that, depending on the precise synthesis conditions (rate of cycling, temperature, size of crystals, time of measurement after synthesis), the superstructure peaks in  $\text{Na}_{2/3}\text{FePO}_4$  can, if present, be of a greater or lesser intensity. It is thus all the more understandable that such a superstructure can rarely be obtained or could easily be missed in

$\text{Li}_{2/3}\text{FePO}_4$ . Dodd *et al.* nevertheless already pointed out an anomaly around the composition  $\text{Li}_{0.6}\text{FePO}_4$  of the phase diagram.<sup>48</sup> The same authors also measured temperature-dependent Mössbauer spectra for this same compound, and observed a rapid evolution of isomer shifts starting around  $150^\circ\text{C}$ .<sup>49</sup> Finally, from DSC measurements, Delacourt *et al.* had already noticed that a transition was occurring around  $180^\circ\text{C}$ - $220^\circ\text{C}$  for intermediate compositions.<sup>15</sup> It is tempting to attribute this unexplained transition to the complete mobility of lithium ions in the channels to switch from the superstruc-

ture phase towards the solid solution, a transition occurring around 250°C in  $\text{Na}_{2/3}\text{FePO}_4$ .

In the search for a similar intermediate composition, Yamada and col.<sup>50</sup> were able to synthesize a single phase with a formulation given as  $\text{Li}_{0.6}(\text{Fe}^{\text{III}}_{0.4}\text{Fe}^{\text{II}}_{0.6})\text{PO}_4$ . The corresponding X-Ray diffraction pattern was fully indexed with a monoclinic unit cell but, astonishingly, this unit cell had a volume three times larger than that of the “usual” Pnma one. The existence of a supercell was demonstrated by selected area electron diffraction with the presence of extra spots. We will discuss this point a little further on (see below), but to the best of our knowledge with respect to this system, it is likely that the reported phase actually corresponds to the charge ordered composition,  $\text{Li}_{2/3}\text{FePO}_4$ . More recently, Orikasa *et al.*<sup>29</sup> used time-resolved XRD measurements to study the structural evolution of the  $\text{Li}_x\text{FePO}_4$  system during battery cycling. At high current fluxes, a new crystalline and metastable phase is observed, with an intermediate composition close to  $\text{Li}_{2/3}\text{FePO}_4$  ( $\text{Li}_x\text{FePO}_4$  with  $x = 0.6\text{--}0.75$ ).

**Structural investigation of  $\text{Li}_{2/3}\text{FePO}_4$  by DFT calculations.** For the lack of better experimental knowledge concerning this metastable lithiated phase, it was decided to study the  $\text{Li}_{2/3}\text{FePO}_4$  composition from a theoretical aspect only. Structural optimizations were guided by DFT calculations at the GGA+U level. The  $\text{Na}_{2/3}\text{FePO}_4$  structural type was used as an initial estimate for the lithiated phase. Using calculation parameters similar to those of the sodium phase (k-point grid, plane wave energy cut-off, U parameters), a full cell relaxation was performed. Both atomic positions and cell parameters were thus relaxed in order to minimize the stress tensor and atomic forces below 0.02 eV/Å. The resulting structural parameters for  $\text{Li}_{2/3}\text{FePO}_4$  are given in Table 3. A monoclinic unit cell (P2<sub>1</sub>/n space group) with the following unit cell parameters is obtained:  $a = 18.0398$  Å,  $b = 4.7967$  Å,  $c = 11.9975$  Å and  $\beta = 120.618^\circ$ . BVS values are also reported and, upon consideration, one is entirely confident in the validity of this hypothetical structure. These values indeed fit perfectly with what is expected: a  $\text{Fe}^{\text{II}}/\text{Fe}^{\text{III}}$  charge ordering is observed in this compound, together with a Li/vacancy ordering along the channels.

Coming back to the unit cell proposed for  $\text{Li}_{0.6}(\text{Fe}^{\text{III}}_{0.4}\text{Fe}^{\text{II}}_{0.6})\text{PO}_4$  by the Yamada group, we have:  $a = 11.8646(7)$  Å,  $b = 4.7552(1)$  Å,  $c = 15.6291(6)$  Å and  $\beta = 100.373(2)^\circ$ .<sup>50</sup> By applying an adequate matrix transformation ( $\mathbf{a}' = \mathbf{a} + \mathbf{c}$ ,  $\mathbf{b}' = \mathbf{b}$ ,  $\mathbf{c}' = -\mathbf{a}$ ) in order to obtain the new  $\mathbf{a}$  parameter along the channel direction, one finds a new monoclinic unit cell with  $a = 17.8399$  Å,  $b = 4.7552$  Å,  $c = 11.8646$  Å and  $\beta = 120.485^\circ$ . This transformed monoclinic cell can be directly compared to the optimized one with an overestimation of 1%, which is in the expected range for GGA+U calculations. We can thus deduce that: 1) The phase reported by the Yamada is more likely to have a  $\text{Li}_{2/3}(\text{Fe}^{\text{III}}_{1/3}\text{Fe}^{\text{II}}_{2/3})\text{PO}_4$  composition rather than a  $\text{Li}_{0.6}(\text{Fe}^{\text{III}}_{0.4}\text{Fe}^{\text{II}}_{0.6})\text{PO}_4$  one, the former having a  $\text{Fe}^{\text{II}}/\text{Fe}^{\text{III}}$  ratio compatible with previous measurements; and 2) Considering the rather good correlation between these optimized cell parameters and the experimental ones, one can argue that the optimized structure we propose for  $\text{Li}_{2/3}\text{FePO}_4$  is reasonably accurate. The resulting experimental cell parameters were used as a constraint in a second DFT optimization, in which only atomic positions were relaxed. The ensuing atomic parameters, also given in Table 3, can consequently be used as is for explaining the experimental XRD pattern reported by the Yamada group.

**Local environment and charge ordering by Mössbauer spectroscopy.** In order to confirm the  $\text{Fe}^{\text{II}}/\text{Fe}^{\text{III}}$  charge ordering in  $\text{Na}_{2/3}\text{FePO}_4$ , as already evidenced by the bond valence calculation (Table 1), <sup>57</sup>Fe Mössbauer spectroscopy experiments were performed on  $\text{Na}_{2/3}\text{FePO}_4$  and compared to the end members,  $\text{NaFePO}_4$  and  $\text{FePO}_4$ . Figure 6a shows the spectra (experimental and fitted) recorded for the three above-mentioned samples. The hyperfine parameters deduced from the refinements, namely the isomer shift (IS) and quadrupole splitting (QS), are given in Table 4. With respect to the end members, the two different valence  $\text{Fe}^{\text{II}}$  and  $\text{Fe}^{\text{III}}$ , characteristic of triphylite and heterosite, show distinct IS (~1.2 mm/s and ~0.4 mm/s, respectively) and QS (~2.8 mm/s and 1.5 mm/s, respectively), which corresponds well with previous reports.<sup>49,51</sup> On the  $\text{NaFePO}_4$  spectrum, a minor  $\text{Fe}^{\text{III}}$  contribution (IS ~ 0.4 mm/s and QS ~ 0.9 mm/s) indicates an incomplete reduction up to the composition  $\text{Na}_{0.96}\text{FePO}_4$ .<sup>52</sup> Hyperfine

parameters such as these correspond to high spin  $\text{Fe}^{\text{III}}$  in an octahedral environment, and were also previously observed in  $\text{Li}_x\text{FePO}_4$  solid solution compounds.<sup>15,49</sup>

Room temperature (RT) experiments for  $\text{Na}_{2/3}\text{FePO}_4$  show signals that are in disagreement with the expected site distribution inferred from the structural determination. If the hyperfine parameters related to  $\text{Fe}^{\text{III}}$  are those expected, and the amount of  $\text{Fe}^{\text{III}}$  vs.  $\text{Fe}^{\text{II}}$  (35% of  $\text{Fe}^{\text{III}}$ ) is compatible with a  $\text{Na}_{2/3}\text{FePO}_4$  composition, then the  $\text{Fe}^{\text{II}}$  component indicates the existence of two very distinct  $\text{Fe}^{\text{II}}$  distributions (QS  $\sim 1.8$  mm/s and QS  $\sim 2.5$  mm/s), as shown from the fit in Figure 6a and highlighted by the QS distribution in Figure 6b. Most importantly, these two  $\text{Fe}^{\text{II}}$  “environments” appear in an approximate 30/70 ratio, whereas a 50/50 proportion is expected in the structure refined from XRD measurements.

A recent study of the  $\text{Na}_x\text{FePO}_4$  phase diagram ( $0 < x < 1$ )<sup>20</sup> noted very similar behavior, also with two distinct  $\text{Fe}^{\text{II}}$  sites for the  $\text{Na}_{2/3}\text{FePO}_4$  composition, which they named site A and site B. They too observed a deviation from the ideal 50/50 expected ratio (40/60 ratio), together with an abnormally small QS value for site A (1.7 mm/s compared to 2.6 mm/s for site B). Consequently, our RT Mössbauer experiments on the  $\text{Na}_{2/3}\text{FePO}_4$  composition are consistent with those published by Lu *et al.*,<sup>20</sup> despite our lower spectral resolution. As a remark, Lu *et al.* attributed the small QS value of the A site to a highly distorted  $\text{Fe}^{\text{II}}$  environment with a low effective coordination number (ECoN),<sup>20</sup> thus a site with a local environment very dissimilar to the one in the  $\text{NaFePO}_4$  compound.

**Table 3.** DFT optimized structural parameters for  $\text{Li}_{2/3}\text{FePO}_4$ .

Atomic position and cell optimization <sup>a</sup>					Atomic position only optimization <sup>b</sup>				
Atom	x	y	z	BVS <sup>c</sup>	x	y	z	BVS <sup>c</sup>	
Fe1	0.1568	0.9638	0.2180	2.00	0.1571	0.9648	0.2194	2.00	
Fe2	0.5089	0.0144	0.7830	3.01	0.5086	0.0161	0.7815	3.01	
Fe3	0.8220	0.9626	0.2219	1.98	0.8226	0.9626	0.2231	1.99	
Li1	0.6651	0.0022	0.5000	1.00	0.6648	0.0013	0.5009	1.00	
Li2	0.8395	0.9816	0.4977	1.00	0.8391	0.9845	0.4987	1.00	
P1	0.2174	0.4205	0.4065	5.03	0.2181	0.4194	0.4080	5.03	
P2	0.4501	0.5775	0.6033	4.99	0.4497	0.5802	0.6007	4.99	
P3	0.8868	0.4152	0.4072	4.99	0.8874	0.4136	0.4087	5.00	
O1	0.2185	0.7402	0.4026	-1.95	0.2190	0.7412	0.4051	-1.95	
O2	0.4520	0.2596	0.6213	-2.01	0.4512	0.2598	0.6172	-2.00	
O3	0.8778	0.7314	0.3984	-2.02	0.8795	0.7321	0.4011	-2.00	
O4	0.0973	0.1675	0.0384	-1.99	0.0976	0.1762	0.0414	-1.99	
O5	0.5665	0.8099	0.9500	-2.03	0.5656	0.8042	0.9479	-2.02	
O6	0.7659	0.2005	0.0454	-2.02	0.7663	0.2054	0.0474	-2.02	
O7	0.1233	0.2936	0.3378	-1.96	0.1232	0.2904	0.3376	-1.98	
O8	0.7421	0.7215	0.6687	-2.02	0.7408	0.7224	0.6678	-2.03	
O9	0.7969	0.2614	0.3394	-2.03	0.7965	0.2612	0.3400	-2.03	
O10	0.4046	0.7337	0.6699	-2.03	0.4037	0.7357	0.6684	-2.03	
O11	0.4582	0.2874	0.3164	-2.00	0.4579	0.2844	0.3177	-2.01	
O12	0.0687	0.7040	0.6659	-1.95	0.0681	0.7083	0.6658	-1.96	

<sup>a</sup>P2<sub>1</sub>/n space group, optimized cell parameters: a = 18.0396 Å, b = 4.7967 Å, c = 11.9975 Å,  $\beta = 120.617^\circ$ . See computational part for details about the DFT optimization. <sup>b</sup>Transformed experimental cell parameters:<sup>50</sup> a = 17.8399 Å, b = 4.7552 Å, c = 11.8646 Å,  $\beta = 120.485^\circ$ . <sup>c</sup>Bond valence sums (BVS) calculated according to Brown and Altermatt<sup>41</sup>, and Brese and O’keeffe.<sup>42</sup>

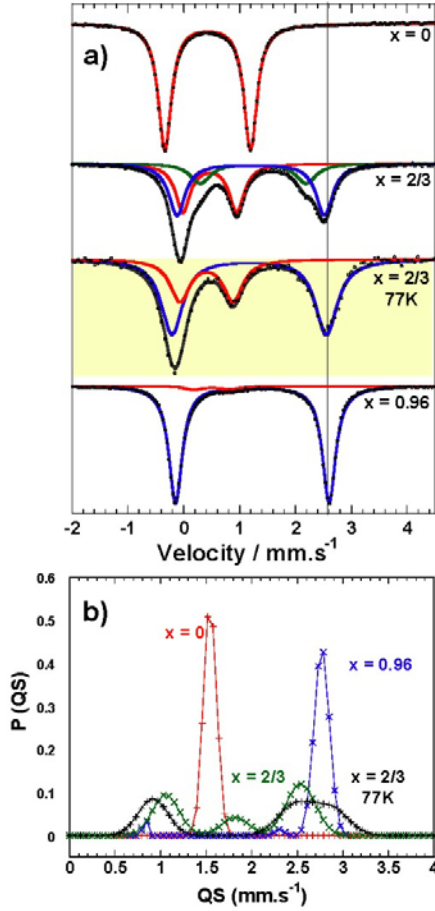


**Figure 6.** (a) Mössbauer spectra for  $\text{Na}_x\text{FePO}_4$ . From top to bottom, Mössbauer spectra for  $\text{FePO}_4$ ,  $\text{Na}_{2/3}\text{FePO}_4$  (at room temperature),  $\text{Na}_{2/3}\text{FePO}_4$  (at 77K), and  $\text{NaFePO}_4$ . Contributions to the signal for  $\text{Fe}^{\text{III}}$  and  $\text{Fe}^{\text{II}}$  are given in red and blue, respectively. In the case of  $\text{Na}_{2/3}\text{FePO}_4$  (at room temperature), a second contribution for  $\text{Fe}^{2+}$  is detected and its contribution is presented in green. Extracted numerical data from these spectra (isomer shifts and quadrupole splittings) are given in Table 4 and compared to DFT calculations. (b) Quadrupole splitting distribution of the Mössbauer spectra shown in (a).

Since valence fluctuation at the Mössbauer time scale had already been demonstrated in disordered  $\text{Li}_x\text{FePO}_4$ ,<sup>49,53</sup> experiments at liquid nitrogen (LN) temperature were carried out. The resulting spectrum is also presented in Figure 6a, and a more uniform  $\text{QS}(\text{Fe}^{\text{II}})$  distribution is now observed in Figure 6b. The latter can be fitted using two Gaussians in a 45/55 proportion, averaged at 2.5 mm/s and 2.9 mm/s, respectively. This result is now compatible with the XRD data, as the Fe1 and Fe3 sites for  $\text{Fe}^{\text{II}}$  ions in  $\text{Na}_{2/3}\text{FePO}_4$  present very similar local environments (Table 2). The  $\text{QS}(\text{Fe}^{\text{II}})$  values are now in a range compatible with the ECoN obtained on the DFT opti-

mized structure. Indeed, according to Lu *et al.*,<sup>20</sup> and considering that the QS values are close to those of  $\text{NaFePO}_4$ , ECoN of about 5.5 are expected. In order to be more quantitative and to assess the expected differences in IS and QS for Fe1 and Fe3, the DFT optimized structure was introduced into an all-electron DFT code, namely WIEN2k,<sup>36</sup> which has been proven to give accurate results for electron density at the nucleus as well as for electrical field gradients. As per the procedure given in the experimental part, theoretical IS and QS parameters were calculated. They are compared to the experimental ones in Table 4, along with those for  $\text{FePO}_4$  and  $\text{NaFePO}_4$ .

Considering the good general correlation to reference compounds, the reasonably similar QS calculated for Fe1 and Fe3 can be considered as in accordance with the broad experimentally-observed  $\text{Fe}^{\text{II}}$  component, with two rather close values. The slightly smaller QS value calculated for the Fe1 site can be explained by the larger distortion of the  $\text{Fe}(1)\text{O}_6$  octahedron compared to the  $\text{Fe}(3)\text{O}_6$  one: larger DIndex, QELong, BAngleVar, and smaller ECoN (see Table 2). Our WIEN2k DFT calculations are also rather accurate as they reproduce the IS and QS values of the  $\text{Fe}^{\text{III}}$  sites. The overall picture of charge ordering is thus consistent.

The temperature dependence of the Mössbauer signal in the  $\text{Li}_x\text{FePO}_4$  solid solution materials was explained by rapid electron dynamics and fast valence fluctuations caused by small-polaron hopping.<sup>49,53-55</sup> Is a fast valence fluctuation already present at RT in  $\text{Na}_{2/3}\text{FePO}_4$ ? The answer is probably no according to the explanations given below. Indeed, the most important difference between these two families is the temperature at which significant deviations are observed for QS and IS. With regard to the disordered  $\text{Li}_{0.6}\text{FePO}_4$  compound, one has to go above 100°C to find a significant variation of QS (above 150°C for IS), and no matter which  $\text{Li}_x\text{FePO}_4$  composition is used,<sup>55</sup> nothing particularly observable can be found below 100°C. At RT, the Mössbauer spectra of all the  $\text{Li}_x\text{FePO}_4$  solid solutions can be very easily interpreted, with two quadrupole-split doublets very similar to those of  $\text{Fe}^{\text{III}}$  in  $\text{FePO}_4$  and  $\text{Fe}^{\text{II}}$  in  $\text{LiFePO}_4$ .<sup>55</sup> In the case of  $\text{Na}_{2/3}\text{FePO}_4$ , however, the RT measurement already shows strong deviation from the expected quadrupole-split doublets. One has to go down to LN temperature in order to obtain an easily interpret-

able Mössbauer signature. Concerning the evolution of the IS values, no significant change is however detected between RT and LN. Two sets of values in the (1/3, 2/3) proportion are observed and correspond very well with the values expected for Fe<sup>III</sup> and Fe<sup>II</sup>, respectively. Furthermore, only the QS of the second Fe<sup>II</sup> site in Table 4 (see also Figure 6b) is affected by the dynamical effect at RT. From the temperature dependence of the X-ray diffraction data (see the Supporting information), it has been shown that the sodium is delocalized above 250°C with the disappearance of the superstructure. Between 100°C and 250°C, structural reorganization exists on the sodium sites and lead to an improvement of the long-range sodium/vacancy ordering.

According to our structural model, the iron charge-ordering is directly coupled to the sodium/vacancy ordering. One could perhaps deduce from this that, no iron valence fluctuation should exist at RT, which is also inferred by analysis of the IS values. Valence fluctuations do however appear at times when approaching the transition temperature of 250°C. A study of this Mössbauer spectral evolution on a wider temperature domain (from LN up to 250°C, for instance) would probably have yielded more information on the thermally-activated electronic process, but this was beyond the scope of the present paper.

**Table 4.** Comparison of experimental Mössbauer parameters with theoretical ones for FePO<sub>4</sub>, Na<sub>2/3</sub>FePO<sub>4</sub> and NaFePO<sub>4</sub>.

		Experiments		DFT calculations				
		IS (mm/s)	QS (mm/s)	IS (mm/s)	QS (mm/s)	$\rho(A)-\rho(\alpha-Fe)^a$ (a.u. <sup>-3</sup> )	$V_{zz}^b$ (10 <sup>21</sup> V/m <sup>2</sup> )	
FePO <sub>4</sub>	Fe <sup>III</sup>	0.43	1.54	0.53	1.48	-1.82	-9.13	
<sup>c</sup> Na <sub>2/3</sub> FePO <sub>4</sub>	Fe <sup>III</sup>	0.41 (0.46)	0.92 (1.06)	0.61	0.78	-2.08	4.82	Fe2
	Fe <sup>II</sup>	1.21 (1.20)	2.47 (2.54)	1.25	2.37	-4.28	-15.43	Fe1
	Fe <sup>II</sup>	1.25 (1.24)	2.87 (1.82)	1.25	2.50	-4.31	14.65	Fe3
NaFePO <sub>4</sub>	Fe <sup>II</sup>	1.23	2.78	1.27	2.66	-4.38	16.45	

<sup>a</sup>Electron densities at the nucleus for the various Fe sites. Differences are calculated with respect to metallic bcc  $\alpha$ -Fe. <sup>b</sup>Major component of the electric field gradient tensor. <sup>c</sup>Mössbauer parameters were measured at 77K. Room temperature values are given between parentheses.

The Ingalls theory<sup>56</sup> can be used to substantiate the difference in the thermal behavior between QS(Fe<sup>II</sup>) and QS(Fe<sup>III</sup>). The high spin configuration of Fe<sup>III</sup> implies that each of the five 3d orbitals is occupied by an electron, giving an approximately spherical shell. Hence, no variation of EFG upon thermal excitation is expected for Fe<sup>III</sup>. On the contrary, the sixth electron of Fe<sup>II</sup> has the possibility of occupying different orbitals, and thus of changing between these orbitals on the time scale of the Mössbauer experiment. Accordingly, upon thermal excitation, the result of this theory offers a more isotropic charge distribution of Fe<sup>II</sup>, and therefore a reduction of the EFG (i.e. QS). The Ingalls theory is thus well-suited for explaining the Mössbauer signatures of Na<sub>2/3</sub>FePO<sub>4</sub>. It was not, however, considered to be relevant in the case of Li<sub>x</sub>FePO<sub>4</sub>,<sup>54</sup> and an explanation was found in fast valence fluctuations caused by small-polaron hopping.

Nevertheless, the relaxation process observed at RT on Fe<sup>II</sup> sites can also be correlated with some Na ion mobility already present at room temperature. Even if the loss of superstructure peaks, which corresponds to important displacements between the sodium sites, is only detected at 250°C by X-ray diffraction, the root mean square displacements (RMSD) of the alkaline cations are probably large enough at RT to have a noticeable effect on the surrounding oxygen atoms. Those oxygen atoms are also shared with the FeO<sub>6</sub> units. Single crystal diffraction experiments at different temperatures are probably necessary in order to be more quantitative on the RMSD evolution of the sodium sites, but by looking at the Na/vacancies neighborhood of the Fe sites one can already establish a correlation with the Mössbauer sensitivity: the larger the number of neighboring sodium atoms, the stronger the sensitivity. In fact, Fe<sup>III</sup> (Fe2) sites are surrounded by 3 Na and 3 vacancies, while Fe<sup>II</sup> sites have more Na around them: 4



Na and 2 vacancies, and 5 Na and 1 vacancy, for Fe1 and Fe3, respectively.

**Formation energies and electrochemical potential calculations.** In order to obtain a better perspective on the thermodynamic at work for Na or Li insertion in  $\text{FePO}_4$ , total-energy calculations were performed with the VASP code. Thanks to our experimental work, the partially intercalated ordered structure can be considered, which can otherwise easily be missed by a systematic search.<sup>20,50</sup> Total energies are reported in Table 5 for all the compositions, together with the formation energies of the intermediate ones.

**Table 5.** Total energies, formation energies, and electrochemical potentials obtained from DFT calculations

		Li	Na
Total energies (eV/FU)	A	-1.900	-1.310
	$\text{FePO}_4$	-42.821	
	$\text{AFePO}_4$	-48.025	-46.961
	$1/3\text{FePO}_4 + 2/3\text{AFePO}_4$	-46.290	-45.581
	$\text{A}_{2/3}\text{FePO}_4$	-46.283	-45.600
Formation energy (meV/FU)	$\text{A}_{2/3}\text{FePO}_4$	+7	-19
	$\text{A}_{2/3} + \text{FePO}_4 \leftrightarrow \text{A}_{2/3}\text{FePO}_4$	3.293 <sup>a</sup>	<b>2.874</b> (2.972 <sup>b</sup> )
Electrochemical potential (V) (vs. $\text{Li}^+/\text{Na}^+$ )	$\text{A}_{1/3} + \text{A}_{2/3}\text{FePO}_4 \leftrightarrow \text{AFePO}_4$	3.325 <sup>a</sup>	<b>2.773</b> (2.869 <sup>b</sup> )
	$\text{A} + \text{FePO}_4 \leftrightarrow \text{AFePO}_4$	<b>3.303</b> (3.422 <sup>b</sup> )	2.830 <sup>a</sup>

<sup>a</sup>These electrochemical potentials are calculated, although not experimentally observed. <sup>b</sup>Experimental values for  $\text{Li}_x\text{FePO}_4$  and  $\text{Na}_x\text{FePO}_4$  are given between parentheses and are taken from Dreyer *et al.*<sup>57</sup> and Moreau *et al.*,<sup>16</sup> respectively.

As suspected from the electrochemical behaviors, the  $\text{Li}_{2/3}\text{FePO}_4$  composition is found to be metastable while the  $\text{Na}_{2/3}\text{FePO}_4$  corresponds to a thermodynamically stable phase. However, the fairly small stabilization found for  $\text{Na}_{2/3}\text{FePO}_4$  (-19 meV/FU) is compatible with the disappearance of the sodium/vacancy ordering at intermediate temperature (250°C). Concerning  $\text{Li}_{2/3}\text{FePO}_4$ , the very small destabilization calculated from DFT (+7 meV/FU) is in fairly good agreement with what was proposed by Malik *et al.*<sup>17</sup> for their most stable configuration of the  $\text{Li}_{0.66}\text{FePO}_4$  composition using a large unit cell ( $2 \times 3 \times 3$  the Pnma cell). This small positive value for the formation energy, well below  $kT$  at RT, can lead to a stabiliza-

tion of the intermediate  $\text{Li}_{2/3}\text{FePO}_4$  phase during fast electrochemical experiments.<sup>29</sup> Electrochemical potentials are also given and are similar to those reported by the Ceder group for lithium intercalation in  $\text{FePO}_4$ ,<sup>3</sup> and to our previously published calculations for the sodium intercalation in  $\text{FePO}_4$ .<sup>16</sup>

The calculated electrochemical potentials are very close to the experimental ones, with a fairly small underestimation: 100 and 120 meV for the sodium and lithium intercalation processes, respectively. Furthermore, a 100 meV potential difference is calculated between the two plateaus in the case of sodium, which is exactly what is observed experimentally.<sup>16</sup>

**Implication for the intercalation process.** The resolution of the  $\text{A}_{2/3}\text{FePO}_4$  intermediate composition structure of ( $\text{A} = \text{Li}, \text{Na}$ ) can now be used to propose an improved view of the intercalation process of alkali ions in  $\text{FePO}_4$ . This discussion is especially pertinent in the sense that particular *operando* behaviors have been observed in both cases (Li and Na intercalation).<sup>21,29</sup> As already demonstrated,<sup>40,58</sup> the ion diffusion path proceeds via the channels along the **b** direction of the Pnma structure. The domino-cascade model further assumes a rapid progression of the intercalation by a successive filling of the **bc** planes of the Pnma structure.<sup>13</sup> A first implication of the possible generalized *operando* intercalation via an intermediate  $\text{A}_{2/3}\text{FePO}_4$  phase is that the successive filling of the  $(\text{bc})_{\text{Pnma}}$  planes is driven by the formation of the  $(10\bar{1})_{\text{Pnma}}$  dense plane discussed above and materialized in Figure 7a.

From this Figure, it can be understood that the filling of a channel in the  $(\text{bc})_{\text{Pnma}}$  plane is highly dependent on the presence of an ion (or an empty site) in the channel in the next  $(\text{bc})_{\text{Pnma}}$  plane in the  $\text{a}_{\text{Pnma}}$  direction. The dense ordering in this  $(10\bar{1})_{\text{Pnma}}$  plane imposes that when two ions are intercalated in one channel, then solely one ion can be intercalated in the next channel in the  $[101]_{\text{Pnma}}$  direction, and none can be intercalated in the channel after next in this same direction. This same interaction prevents a further intercalation of ions in the first channel that we just described, and allows for ions to be intercalated in the two other channels. As a result, the ordering of two successive ions for one empty site along the **b** channels can be viewed as ensuing from the existence of the  $(10\bar{1})_{\text{Pnma}}$  dense plane. Such ordering in a channel would

otherwise have been difficult to justify. This vacancy ordering is easily visible in the  $(ab)_{Pnma}$  plane (Figure 7c) by using a projection along  $c_{Pnma}$ .

We believe that the identification of this dense plane provides the driving force for the propagation of the domino-cascade in the  $a_{Pnma}$  direction. We could further speculate that the crystal would intercalate, not necessarily by involving one  $(bc)_{Pnma}$  plane after another, but by accommodating more  $(bc)_{Pnma}$  planes, together and in a more cooperative manner.

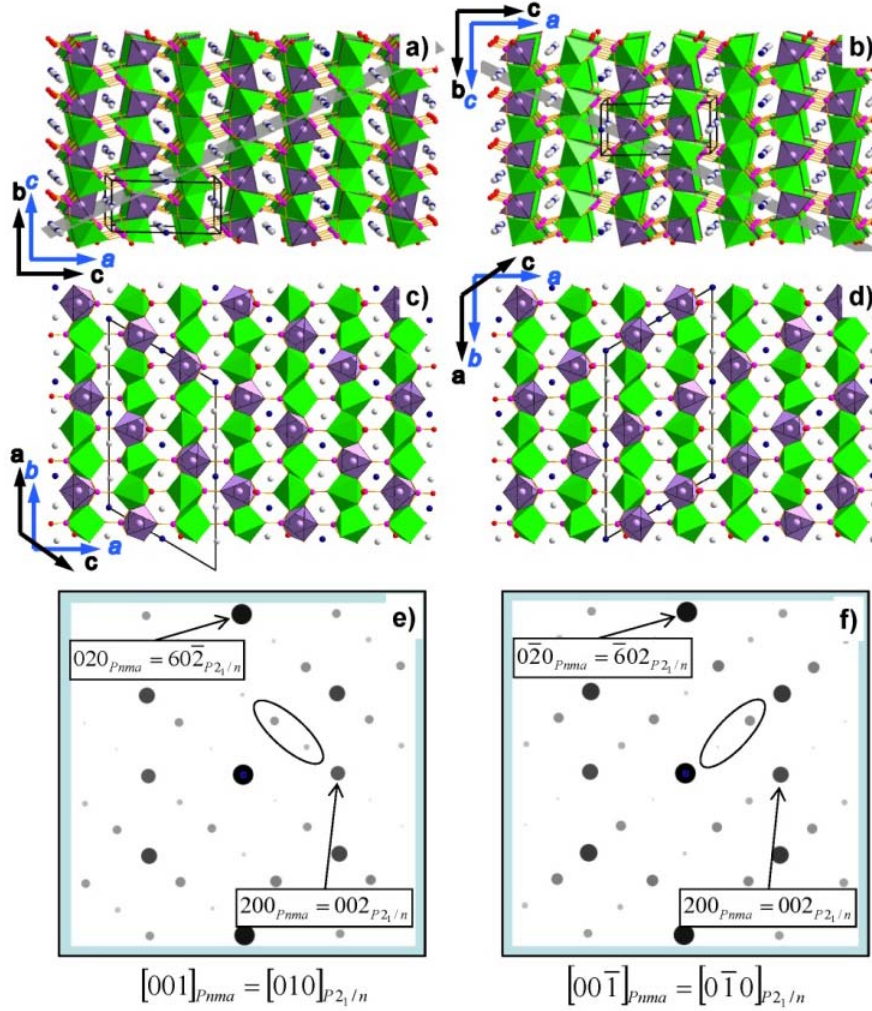


**Figure 7.**  $Na_{2/3}FePO_4$  structure viewed along  $\pm a_{p21/n}$  directions (a) and (b), and  $\pm b_{p21/n}$  directions (c) and (d).  $FeO_6$  octahedra are represented in light green ( $Fe^{II}$ ) and purple ( $Fe^{III}$ ). Sodium atoms (in light grey) and vacancies (in blue) are situated in the channels along the  $a_{p21/n}$  direction. The coordinate systems of the monoclinic and orthorhombic unit cells are shown in black and blue, respectively. A dense intercalation plane is shown in (a) and (b). (e) and (f) Simulated patterns using the JEMS program for the zone axis corresponding to the orientation of (c) and (d), respectively.

The core of the domino-cascade consists in the existence of a small polaron that can propagate long the  $c_{Pnma}$  axis<sup>13</sup> which, along with a preferred diffusion in the  $b$  channels, gives rise to a rapid  $(bc)_{Pnma}$  plane intercalation. In fact, the intermediate  $A_{2/3}FePO_4$  structure preserves this kind of distortion minimization along the  $c_{Pnma}$  direction since, in this direction,  $FeO_6$

octahedra are all identical (Figure 7a). The existence of the  $A_{2/3}FePO_4$  structure can thus be viewed as further confirmation of the small polaron model.

Another interesting consequence of the existence of the  $(10\bar{1})_{Pnma}$  dense plane is that it might play a role in the nu-

cleation process of the intercalation. If one considers that such a plane exists at the surface of the crystal, intercalation within the **b** channels would then be all the more favored since it could proceed with the assistance of adsorbed ions. This may be of practical interest since Wang *et al.*<sup>59</sup> have shown that the (101) surface, and the  $(\pm 1\ 0\ \pm 1)$  symmetry related ones (mmm point group), have the lowest energy among the non-principal directions, as well as the lowest redox potential for the extraction of Li (after the (010) surface). We may thus expect that a crystal synthesis leading to a large amount of (101) surfaces would intercalate ions very rapidly. Controlling the crystal shape is not an easy task, although different approaches can be conceived for this purpose. The first one, a top-down technique, would consist in the grinding of large  $\text{LiFePO}_4$  particles. However, according to available literature,<sup>60</sup> cleavage is expected to preferentially occur along the (1 0 0) or (0 1 0) surfaces. A more elegant bottom-up approach would be to directly design the crystal shape from the synthesis. Some pioneering work on the  $\text{LiFePO}_4$  compound was carried out by Kanamura *et al.*<sup>61</sup> using hydrothermal conditions. They obtained a plate-like crystal shape with an enhancement of the (0 1 0) faces. Using a pulsed laser deposition technique, (1 0 0) surfaces were also obtained by Hirayama *et al.*<sup>62</sup> who grew oriented epitaxial thin film of  $\text{LiFePO}_4$ . However, to our best knowledge, nobody seems to have focused on the preparation of  $\text{LiFePO}_4$  particles with other orientations for the crystal faces. One possible solution for promoting the (1 0 1) faces could be to use electrodeposition and the preferential adsorption, and masking techniques developed by Choi and col.<sup>63</sup> According to the surface properties calculated for  $\text{LiFePO}_4$ ,<sup>59</sup> masking the (1 0 1) surfaces can help in promoting them with respect to the (2 0 1), which is the face with the lowest energy.

It should be mentioned that two different orientations of the dense plane with respect to the  $(\mathbf{ab})_{\text{Pnma}}$  plane could be chosen (see Figures 7a and 7b with a  $\pm 25.6^\circ$  tilt along the  $\mathbf{b}_{\text{Pnma}}$  axis). This has multiple implications for the intercalation process: (i) Once the intercalation has started within a  $(\mathbf{bc})_{\text{Pnma}}$  plane or  $\mathbf{b}_{\text{Pnma}}$  channel, the intercalation can then proceed either in the  $\mathbf{a}_{\text{Pnma}}$  or the  $-\mathbf{a}_{\text{Pnma}}$  direction. This could give the crystal some leeway, allowing for rapid intercalation; (ii) The interaction between channels is a key parameter of the intercalation pro-

cess, and defects in other channels could impede this process, not only because the channel would be blocked (due to A-Fe anti-site defects for example)<sup>40</sup> but because it prevents the formation of the dense plane and thus the minimization of energy; (iii) If (101) surfaces exist in the intercalating/deintercalating crystals, as expected from the Wulff shape of  $\text{LiFePO}_4$ ,<sup>59</sup> the nucleation could proceed from these surfaces. Whereas the (101) and the  $(10\bar{1})$  surfaces are equivalent in the Pnma structure, such is not the case in the monoclinic cell (Figures 7a and 7b). Consequently, if nucleation starts simultaneously on such surfaces on opposite sides of the crystal, a twinning is bound to appear, of which the probability will depend upon the size and shape of the crystals, hence on their synthesis route. Two different orientations of the monoclinic unit cell would be observed (Figures 7c and 7d) and two sets of superstructure spots would be obtained (Figures 7e and 7f) in the [010] zone axis of the  $\text{P2}_1/\text{n}$  cell, which is the [001] zone axis of the Pnma structure. This explains the sets of reflections obtained in Fig 2d of Reference 25 very well. The extra reflections forming a square, in between the Pnma structure reflections, are due to the superimposition of two intercalated regions in the same crystal. Since this observation is clearly favored by a large crystal thickness (unrelated nucleation places), the use of 300 kV TEM conditions by Casas-Cabanas *et al.*<sup>25</sup> could explain why we did not observe such twinned crystals (100 kV conditions in our experiment, hence thinner crystals). With respect to intercalation chemistry, it is common knowledge that the consequence of such an intercalation process on the electron diffraction patterns is the lowering of symmetry (for example intercalation of Hg into  $\text{TiS}_2$  inducing a change from hexagonal to monoclinic).<sup>64</sup>

## CONCLUSION

From TEM, X-Ray synchrotron diffractions, DFT calculations and Mössbauer spectroscopy, this work unraveled a 3-fold superstructure for the  $\text{Na}_{2/3}\text{FePO}_4$  intermediate phase of the  $\text{Na}/\text{FePO}_4$  system. This stable superstructure, which is characterized by the occurrence of  $\text{Na}^+$  pair and  $\text{Fe}^{\text{II}}/\text{Fe}^{\text{III}}$  charge ordering, was found to be very useful in pinpointing, for the first time, the description of the isostructural  $\text{Li}_{2/3}\text{FePO}_4$  metastable phase. Further VASP calculations confirmed (de)stabilization energies for  $(\text{Li})\text{Na}_{2/3}\text{FePO}_4$  with intercalation potentials of approximately 100 mV below experimental values. These results were used to propose an improved view of the first order intercalation process in  $\text{FePO}_4$ , taking into account the formation of the  $\text{A}_{2/3}\text{FePO}_4$  phase. This mechanism is based on the existence of the alkali/vacancy dense  $(10\bar{1})_{\text{Pnma}}$  plane, which is associated with the second and third shortest Na-Na distances. We believe that the corresponding strong Na-Na interactions dictate the sequential intercalation of two successive ions for one empty site, not only in the channel  $\mathbf{b}_{\text{Pnma}}$  direction, but also along  $\mathbf{a}_{\text{Pnma}}$  by cooperative filling of  $(\mathbf{bc})_{\text{Pnma}}$  planes. If our generalized mechanism is correct, the results point to the importance of designing grains with a large number of (101) planes, thereby promoting the high-rate performance of Na and Li battery devices.

## ASSOCIATED CONTENT

**Supporting Information.** Synchrotron X-Ray Rietveld refinement data for  $\text{Na}_{2/3}\text{FePO}_4$  with crystallographic information file (CIF); cell parameter evolution for temperature-dependent experiment performed on  $\text{Na}_{2/3}\text{FePO}_4$ ; in situ X-ray diffraction pattern showing the reversible disappearance and appearance of a superstructure peak above and below 250°C, DFT geometry optimization of  $\text{Na}_{2/3}\text{FePO}_4$  and  $\text{Li}_{2/3}\text{FePO}_4$ ; details of calculations and structural features (atomic positions and bond lengths) of the optimized structures. This material is available free of charge via the Internet at <http://pubs.acs.org>.

## AUTHOR INFORMATION

### Corresponding Author

\*E-mail: Florent.Boucher@cncrs-imn.fr

### Present Address

<sup>§</sup>University of Waterloo, Department of Chemistry, 200 University Avenue West, Waterloo, Ontario, Canada N2L 3G1

### Author Contributions

All authors contributed equally to this manuscript.

## Notes

The authors declare no competing financial interest.

## ACKNOWLEDGMENT

The SOLEIL synchrotron X-ray diffraction experiments were made possible through the Proposal No. 20100981. The authors would like to acknowledge the assistance of P. Soudan and E. Elkaim in the synchrotron data acquisition. F. B. gratefully acknowledges J.-M. Perez-Mato for fruitful discussions concerning the 2D pseudo-uniform ordering.

## REFERENCES

- (1) Tarascon, J.; Armand, M. *Nature* **2001**, *414*, 359–367.
- (2) Kang, B.; Ceder, G. *Nature* **2009**, *458*, 190–193.
- (3) Zhou, F.; Kang, K.; Maxisch, T.; Ceder, G.; Morgan, D. *Solid State Commun* **2004**, *132*, 181–186.
- (4) Ravet, N.; Chouinard, Y.; Magnan, J.; Besner, S.; Gauthier, M.; Armand, M. *J Power Sources* **2001**, *97*–8, 503–507.
- (5) Huang, H.; Yin, S.; Nazar, L. *Electrochem Solid St* **2001**, *4*, A170–A172.
- (6) Yamada, A.; Chung, S.; Hinokuma, K. *J Electrochem Soc* **2001**, *148*, A224–A229.
- (7) Padhi, A.; Nanjundaswamy, K.; Goodenough, J. J. *Electrochem Soc* **1997**, *144*, 1188–1194.
- (8) Andersson, A.; Thomas, J. *J Power Sources* **2001**, *97*–8, 498–502.
- (9) Srinivasan, V.; Newman, J. *J Electrochem Soc* **2004**, *151*, A1517–A1529.
- (10) Chen, G.; Song, X.; Richardson, T. *Electrochem Solid St* **2006**, *9*, A295–A298.
- (11) Laffont, L.; Delacourt, C.; Gibot, P.; Wu, M. Y.; Kooyman, P.; Masquelier, C.; Tarascon, J. M. *Chem Mater* **2006**, *18*, 5520–5529.
- (12) Allen, J. L.; Jow, T. R.; Wolfenstine, J. *J Solid State Electr* **2008**, *12*, 1031–1033.
- (13) Delmas, C.; Maccario, M.; Croguennec, L.; Le Cras, F.; Weill, F. *Nat Mater* **2008**, *7*, 665–671.
- (14) Malik, R.; Abdellahi, A.; Ceder, G. *J Electrochem Soc* **2013**, *160*, A3179–A3197.
- (15) Delacourt, C.; Poizot, P.; Tarascon, J.; Masquelier, C. *Nat Mater* **2005**, *4*, 254–260.
- (16) Moreau, P.; Guyomard, D.; Gaubicher, J.; Boucher, F. *Chem Mater* **2010**, *22*, 4126–4128.
- (17) Malik, R.; Zhou, F.; Ceder, G. *Nat Mater* **2011**, *10*, 587–590.
- (18) Robert, D.; Douillard, T.; Boulineau, A.; Brunetti, G.; Nowakowski, P.; Venet, D.; Bayle-Guillemaud, P.; Cayron, C. *ACS Nano* **2013**, *7*, 10887–10894.
- (19) Moreau, P.; Cuisinier, M.; Turpin, B.; Gaubicher, J.; Boucher, F.; Guyomard, D. In *7th International Symposium on Inorganic Phosphate Materials (ISIPM7)*; Argonne US-IL, 2011.
- (20) Lu, J.; Chung, S. C.; Nishimura, S.; Oyama, G.; Yamada, A. *Chem Mater* **2013**, *25*, 4557–4565.
- (21) Gaubicher, J.; Boucher, F.; Moreau, P.; Cuisinier, M.; Soudan, P.; Elkaim, E.; Guyomard, D. *Electrochem. Commun.* **2014**, *38*, 104–106.
- (22) Sun, A.; Manivannan, A. In *BATTERIES AND ENERGY TECHNOLOGY (GENERAL)- 219TH ECS MEETING*; Smart, M.; Manivannan, A.; Kumta, P.; Narayan, S., Eds.; ECS Transactions; Montreal, QC, Canada, 2011; Vol. 35, pp. 3–7.
- (23) Trottier, J.; Hovington, P.; Brochu, F.; Rodrigues, I.; Zaghbi, K.; Mauger, A.; Julien, C. M. In *NANOSTRUCTURED MATERIALS FOR ENERGY STORAGE AND CONVERSION*; Zaghbi, K.; Chiu, W.;

- Ramani, V.; Liaw, B.; Julien, C.; Mustain, W.; VanSchalkwijk, W., Eds.; ECS Transactions; Montreal, QC, Canada, 2011; Vol. 35, pp. 123–128.
- (24) Zaghib, K.; Trottier, J.; Hovington, P.; Brochu, F.; Guerfi, A.; Mauger, A.; Julien, C. M. *J Power Sources* **2011**, *196*, 9612–9617.
- (25) Casas-Cabanas, M.; Roddatis, V. V.; Saurel, D.; Kubiak, P.; Carretero-Gonzalez, J.; Palomares, V.; Serras, P.; Rojo, T. *J Mater Chem* **2012**, *22*, 17421–17423.
- (26) Ellis, B. L.; Nazar, L. F. *Curr Opin Solid St M* **2012**, *16*, 168–177.
- (27) Oh, S.-M.; Myung, S.-T.; Hassoun, J.; Scrosati, B.; Sun, Y.-K. *Electrochem Commun* **2012**, *22*, 149–152.
- (28) Sun, A.; Beck, F. R.; Haynes, D.; Poston, J. A. Jr.; Narayanan, S. R.; Kumta, P. N.; Manivannan, A. *Mater Sci Eng B-adv* **2012**, *177*, 1729–1733.
- (29) Orikasa, Y.; Maeda, T.; Koyama, Y.; Murayama, H.; Fukuda, K.; Tanida, H.; Arai, H.; Matsubara, E.; Uchimoto, Y.; Ogumi, Z. *J Am Chem Soc* **2013**, *135*, 5497–5500.
- (30) Lee, K. T.; Ramesh, T. N.; Nan, F.; Botton, G.; Nazar, L. F. *Chem Mater* **2011**, *23*, 3593–3600.
- (31) Stadelmann, P. A. *JEMS*; CIME: EPFL, Switzerland, 2009.
- (32) Perdew, J. P.; Burke, K.; Ernzerhof, M. *Phys. Rev. Lett.* **1996**, *77*, 3865–3868.
- (33) Kresse, G.; Furthmüller, J. *Phys Rev B* **1996**, *54*, 11169–11186.
- (34) Blöchl, P. E. *Phys. Rev. B: Condens. Matter Mater. Phys.* **1994**, *50*, 17953–17979.
- (35) Kresse, G.; Joubert, D. *Phys. Rev. B: Condens. Matter Mater. Phys.* **1999**, *59*, 1758–1775.
- (36) Blaha, P.; Schwarz, K.; Madsen, G.; Kvasnicka, D.; Luitz, J. *WIEN2k, An Augmented Plane Wave + Local Orbitals Program for Calculating Crystal Properties*; Karlheinz, S., Ed.; Vienna University of Technology, Austria, 2001.
- (37) Petrilli, H.; Blochl, P.; Blaha, P.; Schwarz, K. *Phys Rev B* **1998**, *57*, 14690–14697.
- (38) Pyykkö, P. *Mol Phys* **2008**, *106*, 1965–1974.
- (39) Wdowik, U. D.; Ruebenbauer, K. *Phys Rev B* **2007**, *76*, 155118–6.
- (40) Islam, M.; Driscoll, D.; Fisher, C.; Slater, P. *Chem Mater* **2005**, *17*, 5085–5092.
- (41) Brown, I.; Altermatt, D. *Acta Crystallogr., Sect B: Struct Sci* **1985**, *41*, 244–247.
- (42) Brese, N.; O'keeffe, M. *Acta Crystallogr., Sect B: Struct Sci* **1991**, *47*, 192–197.
- (43) Perez-Mato, J. M. Private discussion, ECSSC14, Bordeaux, France (2013).
- (44) Gonzalez, S.; Perez-Mato, J. M.; Elcoro, L.; Garcia, A. *Phys Rev B* **2011**, *84*, 184106.
- (45) Baur, W. H. *Acta Crystallogr., Sect B: Struct Sci* **1974**, *30*, 1195–1215.
- (46) Robinson, K.; Gibbs, G. V.; Ribbe, P. H. *Science* **1971**, *172*, 567–570.
- (47) Hightower, A.; Ahn, C.; Fultz, B.; Rez, P. *Appl Phys Lett* **2000**, *77*, 238–240.
- (48) Dodd, J. L.; Yazami, R.; Fultz, B. *Electrochem Solid St* **2006**, *9*, A151–A155.
- (49) Dodd, J. L.; Halevy, I.; Fultz, B. *J Phys Chem C* **2007**, *111*, 1563–1566.
- (50) Furutsuki, S.; Chung, S.-C.; Nishimura, S.; Kudo, Y.; Yamashita, K.; Yamada, A. *J Phys Chem C* **2012**, *116*, 15259–15264.
- (51) Andersson, A.; Kalska, B.; Haggstrom, L.; Thomas, J. *Solid State Ionics* **2000**, *130*, 41–52.
- (52) Martin, J. F.; Yamada, A.; Kobayashi, G.; Nishimura, S.; Kanno, R.; Guyomard, D.; Dupre, N. *Electrochem Solid St* **2008**, *11*, A12–A16.
- (53) Ellis, B.; Perry, L. K.; Ryan, D. H.; Nazar, L. F. *J Am Chem Soc* **2006**, *128*, 11416–11422.
- (54) Tan, H.; Fultz, B. *J Phys Chem C* **2011**, *115*, 7787–7792.
- (55) Tan, H. J.; Dodd, J. L.; Fultz, B. *J Phys Chem C* **2009**, *113*, 2526–2531.
- (56) Ingalls, R. *Phys Rev* **1964**, *133*, A787–A795.
- (57) Dreyer, W.; Jamnik, J.; Gohlke, C.; Huth, R.; Moskon, J.; Gaberscek, M. *Nat Mater* **2010**, *9*, 448–453.
- (58) Malik, R.; Burch, D.; Bazant, M.; Ceder, G. *Nano Lett* **2010**, *10*, 4123–4127.
- (59) Wang, L.; Zhou, F.; Meng, Y. S.; Ceder, G. *Phys Rev B* **2007**, *76*, 165435.
- (60) Jung, J.; Cho, M.; Zhou, M. *J Power Sources* **2013**, *243*, 706–714.
- (61) Kanamura, K.; Koizumi, S.; Dokko, K. *J Mater Sci* **2008**, *43*, 2138–2142.
- (62) Hirayama, M.; Yonemura, M.; Suzuki, K.; Torikai, N.; Smith, H.; Watkinsand, E.; Majewski, J.; Kanno, R. *Electrochemistry* **2010**, *78*, 413–415.
- (63) Choi, K.-S. *Dalton Trans.* **2008**, *40*, 5432–5438.
- (64) Sidorov, M.; McKelvy, M.; Sharma, R.; Glausinger, W.; Ganai, P.; Moreau, P.; Ouvrard, G. *Chem Mater* **1995**, *7*, 1140–1152.

#### SYNOPSIS TOC

